The Astrophysical Journal Supplement Series, 262:5 (9pp), 2022 September https://doi.org/10.3847/1538-4365/ac7e53

A CO Survey of the Entire Northern Sky

T. M. Dame and P. Thaddeus[1]
Center for Astrophysics | Harvard & Smithsonian, 60 Garden Street, Cambridge, MA 02138, USA; tdame@cfa.harvard.edu
Received 2022 June 3; revised 2022 June 30; accepted 2022 July 1; published 2022 August 17

Abstract

We present a very large extension of the Galactic plane CO survey of Dame et al. to the entire northern sky ($\delta > -17°$). The extension was carried out with the same telescope as was used for the plane survey, the CfA 1.2 m, and perfectly meshes with its irregular boundaries in latitude. A total of 382,202 CO(1–0) spectra uniformly sample the high-latitude sky with a true-angle spacing of $0\overset{\circ}{.}25$ or better. The final reduced and folded spectra have a uniform sensitivity of 0.18 K in 0.65 km s^{-1} channels and provide a velocity coverage of $\pm$47.1 km s^{-1}. We describe the observational techniques and the data reduction and provide various summary maps of the spatial and velocity distributions of CO emission over the northern sky, and a catalog of the molecular clouds we found there. We also describe the CO spectral line data cubes that we have made available online.

Unified Astronomy Thesaurus concepts: Molecular clouds (1072); Diffuse molecular clouds (381); Interstellar molecules (849); Interstellar line emission (844); Solar neighborhood (1509)

Supporting material: data behind figure, machine-readable table

1. Introduction

The 1.2 m Millimeter-Wave Telescope at the Center for Astrophysics | Harvard & Smithsonian has been observing the $J = 1 - 0$ rotational transition of interstellar carbon monoxide for nearly 50 yr. Working with its twin instrument in Chile, it has produced the most extensive and widely used survey of the entire Galactic plane and all large local clouds (Dame et al. 2001; hereafter DHT) as well as complete surveys of the Large Magellanic Cloud (Cohen et al. 1988) and M31 (Dame et al. 1993). In recent years, while continuing deep observations of particular regions of interest (e.g., Dame & Thaddeus 2011; Lallement et al. 2016), the telescope has also been steadily mapping the sky to ever higher Galactic latitudes. Here we combine the new high-latitude data with the DHT survey to present the first complete CO survey of the entire northern sky at $\delta > -17°$.

Most previous CO observations at high Galactic latitudes have been biased toward regions of optical obscuration (e.g., Magnani et al. 1985) or enhanced infrared emission (e.g., Désert et al. 1988). The only previous CO survey with high-latitude coverage comparable to that presented here was likewise carried out with the CfA 1.2 m telescope and was reported in two papers covering the northern and southern Galactic hemispheres (Hartmann et al. 1998 & Magnani et al. 2000; hereafter the H&M survey). That survey, however, was 16 times less densely sampled than the present one (1° sampling versus 1/4° here), and it employed an unusual "ON-ON" switching strategy that was effective at finding clouds but could not be used to produce a uniform spectral line survey.

Also of note here are the all-sky CO maps recently extracted as "foreground contamination" from the Planck survey (Planck Collaboration 2016). Planck's high-frequency bolometers are so sensitive that they can detect the three lowest rotational transitions of CO even though the widths of these lines are several orders of magnitude narrower than that of the bolometers. Various extraction schemes were employed with different trade-offs in terms of angular resolution, sensitivity, and systematics. Their recommended $J = 1$–0 map (Type 2 in their Table 9) has the same angular resolution as the one presented here, but is ~50% less sensitive. Still, as their Figure 32 shows, the spatial correlation between their map and ours is very good in regions of high CO intensity. A significant drawback of the Planck CO maps, however, is their lack of kinematic information, so they provide no line widths or velocities for the clouds detected.

The present survey, then, is the first uniformly sampled, general-purpose CO spectral line survey of the northern sky, and its utility is significantly enhanced by the fact that it was carried out with the same telescope as that of DHT and perfectly meshes with that survey over its irregular boundaries in latitude. While the present survey will enable numerous studies of the local molecular galaxy, specific studies are not presented here. Rather we will enable such studies by fully describing the survey itself and the data products that are made available.

A brief description of the CfA telescope and of the way the survey was obtained is given in the next section. Section 3 discusses in detail the data processing, which was in some respects the most challenging of any survey conducted with the 1.2 m telescopes. We describe how we modeled and removed the mesospheric CO line from each spectrum even while this line's intensity sometimes varied significantly over short time periods. Extracting as much real emission as possible from the survey was another challenge because most of the observed lines were weak and narrow and were widely scattered both spatially and in velocity. In Section 4 we present and discuss the survey using different projections on the plane of the sky and as a function of velocity, and finally, in Section 5 we describe the data products that are available online.

[1] Died 2017 April 28.

2. Instrumentation and Observations

The 1.2 m telescope has been described in many previous publications, including in particular DHT and references therein. Briefly, its Cassegrain antenna consists of a parabolic primary and hyperbolic secondary that provide a fast diffraction-limited system with an effective f/D of 3.79; the measured beamwidth of 8.′4 and beam efficiency of 0.82 are in good agreement with the predictions of scalar diffraction theory. Its liquid-helium cooled SIS receiver has a single-sideband noise temperature of ∼65 K. Over the normal observing range of elevation (30°−75°), the total system temperature varies from ∼800 to ∼400 K, with acceptable weather variations imposing a scatter of ∼50 K on these values. The telescope is equipped with two 256-channel filter bank spectrometers that are identical except for their channel widths, which are 0.25 and 0.5 MHz. At 115 GHz, the narrower channels provide a velocity resolution of 0.65 km s^{-1} and velocity coverage of 166 km s^{-1}; the wider channels provide half the resolution, but twice the coverage. Observations were taken with both spectrometers centered at an LSR velocity of 0 km s^{-1}.

Spectral lines were calibrated by measuring the receiver response to two thermal sources of known temperature: a blackbody chopper wheel, and the sky (Penzias & Burrus 1973). The temperature near the chopper was measured continuously by the control computer, and the effective blackbody temperature of the sky was calculated using a two-layer atmospheric model (Kutner 1978). The model parameters were determined by sky dipping at the beginning of each observing run and subsequently whenever weather changes caused significant systematic deviations of the sky brightness from the model prediction. Intensities reported here are further divided by the main-beam efficiency to obtain the main-beam brightness temperature $T_{\rm mb}$ (Downes 1989).

Instrumental baseline structure was removed by frequency switching every 1 s by 15 MHz (39 km s^{-1}) and subtracting the data from the two phases. At the high Galactic latitudes of the present observations, both switching phases of all observed lines–including those from the mesosphere–remained within range of even the high-resolution spectrometer. A final rms noise of 0.18 K ($T_{\rm mb}$) in 0.65 km s^{-1} channels was achieved for each scan by measuring the total system temperature at the start of the observation and adjusting the integration time accordingly. Integration times ranged from ∼30 s at high elevations with cold clear weather to ∼4 minutes at low elevations with warm cloudy weather.

The new high-latitude observations consist of 382,202 spectra that cover ∼20,000 deg^2, roughly half of the entire sky and more than double the area of the DHT survey; together, the two surveys cover three quarters of the sky. All observations at $|b| < 50°$ were taken on a $1/4°$ grid in Galactic longitude and latitude. At higher latitudes, the longitude spacing was increased by a multiple of $1/8°$ (approximately one beamwidth and the standard spacing of our survey grids) in order to maintain true-angle spacing in longitude of $\sim 1/4°$ or somewhat better. The longitude intervals used as a function of Galactic latitude are given in Table 1. We did not observe within 1° of the Galactic pole. In order to average out day-to-day calibration variations and for other practical reasons, the total survey area was divided into $10° \times 10°$ regions that were each observed using four interleaved $1/2°$ grids.

Table 1
Longitude Spacing versus Latitude

$\|b\|$ Range (deg)	l Spacing (deg)
0–49.75	0.250
50–59.75	0.375
60–60.75	0.500
70–79.75	0.750
80–85.75	4.000
86–89.00	8.000

3. Data Reduction

Here we describe the treatment of bad spectral channels, baseline fitting, quality assurance, removal of the mesospheric line, sig-ref phase folding, noise suppression, and the meshing of the new data with those of DHT.

The two filter bank spectrometers have proven extremely reliable over decades of use, but on occasion, the response of an individual channel can grow slightly nonlinear with input power. The redundancy provided by the two spectrometers running simultaneously allowed us to correct these bad channels in postprocessing. The intensity measured in any wide channel generally agrees to much better than the instrumental noise with the average of the two narrow channels with which it is aligned. This is because nearly all of the noise originates in the receiver front end, not in the spectrometers. If one of the narrow channels was identified as bad, its intensity in each affected spectrum was adjusted such that the average of the two narrow channels agreed with that of the aligned wide channel. The wide channels were only used for this purpose and were not carried into subsequent stages of the reduction and analysis.

To achieve flat spectral baselines, we fit the spectra with a fifth-order polynomial. In order to substantially improve the overall quality of the fit, we eliminated 25 spectral channels on either end of the spectrum, corresponding to velocities in excess of 67 km s^{-1} in absolute value, well above the velocities expected for all celestial or telluric lines at high latitude. Since the velocities of the telluric line in both frequency-switching phases can be calculated, a 5 km s^{-1} wide window around each was masked from the fit. The rms residual from this fit was then used to mask any channels with absolute intensities greater than three times the noise; this procedure was repeated iteratively until the rms stabilized to <1%. The rms measured for all 56 million spectral channels in the final l-b-v data cube was 0.18 K, in near perfect agreement with the targeted value mentioned in Section 2. A histogram of the rms values measured in each spectrum is shown in Figure 1.

Roughly 3% of the total scans processed were discarded and reobserved owing to conditions indicative of lower data quality or unreliable calibration. These include scans taken at elevations below 26°, with rms noise greater than 0.26 K, and with a difference in total power between the two frequency-switching phases greater than 10 K. Also excluded were scans taken when the measured sky brightness at the time of observation deviated by more than 15% from the two-layer atmospheric model prediction.

Removal of the telluric emission line from CO in the mesosphere was a serious challenge for the present survey. Since the telluric emission appears in every spectrum and the celestial emission is sparse (Section 4), the former accounts for

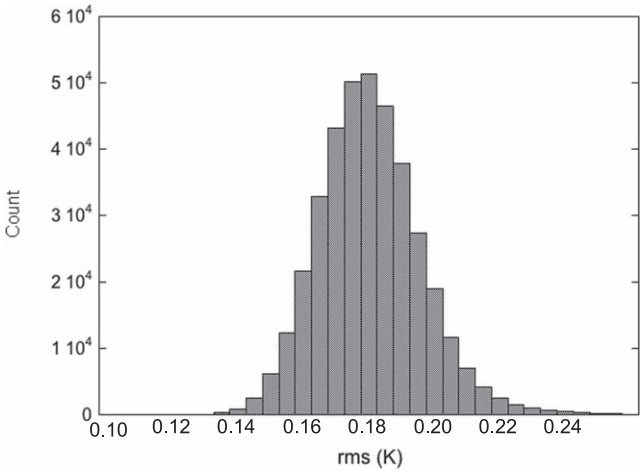

Figure 1. Histogram of the final rms noise in each of the 382,202 spectra in the survey.

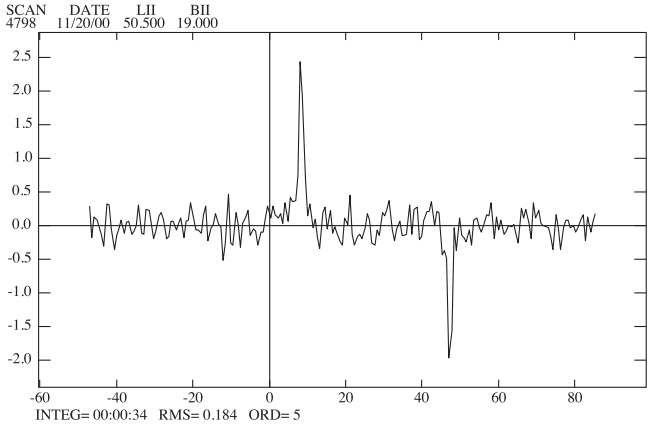

Figure 2. Typical frequency-switched spectrum from the survey, taken at an elevation of 70°.

over 98% of the detected line emission. In a typical frequency-switched spectrum such as the one shown in Figure 2, the line appears twice with opposite signs and separated by the frequency offset of 15 MHz or 39 km s^{-1}. The line of course appears at 0 km s^{-1} in the laboratory frame, but in the LSR frame, it varies with direction on the sky as well as time of day and year. When mapping a particular region or cloud, it is often possible, by observing at the right time of year, to position the telluric line in LSR velocity well away from the celestial CO emission. For the present survey, however, observations were conducted over much of the sky every day, and the celestial emission observed was generally weak and at a velocity that was not known in advance. The intensity and width of the telluric lines were also not known in advance because as we show below, both can vary with time.

In Figure 3 we have shifted the spectra in our survey into the laboratory frame (in which the telluric line appears at 0 km s^{-1}) and have corrected the line intensities to the zenith. The spectra are grouped by observing season and are stacked vertically ordered by scan number. Consequently, within each season, the spectra run from roughly mid-October at the bottom to mid-May at the top. As we show below, the celestial emission is sufficiently weak and sparse to have little effect on this figure.

It is clear from Figure 3 that the telluric CO line varies on many timescales. All years show a seasonal variation, with the lines becoming weaker and narrower in the spring. This is consistent with the photochemical and transport modeling of Solomon et al. (1985), who predicted a very large pole-to-pole gradient in mesospheric CO, with the highest concentrations at the winter pole. Very significant inter-year variations are also evident. Compare, for example, the strong and highly variable lines seen during the 2001–2002 season with the relative weak and quiescent lines in 2009–2010. There are also significant intra-year variations on timescales as short as a few hours. To show this more clearly, a five-day section of the data from the 2001–2002 season is expanded in Figure 4, where we display hour-long averages of the telluric line integrated intensity. Note the smooth factor-of-two rise and fall of the line intensity over the course of just 24 hr. These changes are thought to be more dramatic at higher terrestrial latitudes such as that of our telescope, where meridional transport by planetary waves can produce temporary bursts of CO-rich air from the northern polar vortex (e.g., de Zafra & Muscari 2004; Forkman et al. 2012).

Given the variability of the telluric line, it was necessary to measure its mean profile frequently—by default once per day—and subtract it from all scans taken during that time period. The stability of the line throughout the day was judged using plots similar to the one in Figure 4 (an extreme case of variability). For days with significant variability, mean profiles were determined over shorter time periods, whereas during quiescent periods, generally in the spring, a single profile could be used for multiple days. Since observations on a given day were never spaced closer than $1/2°$ and included multiple $10° \times 10°$ regions that were widely separated on the sky, celestial emission had very little impact on the mean telluric profiles. To remove any influence of celestial emission, we iteratively removed any individual spectral channels that deviated by more than 3σ from the mean telluric profile.

The telluric profile could be well fit using the sum of Gaussian and Lorentzian profiles (a pseudo-Voigt function), the former accounting for the mean Doppler broadening above ~60 km and the latter for the mean pressure broadening at lower altitudes. See, for example, Figure 5, which shows the mean telluric profile for all 51,015 scans taken during the 2001–2002 observing season with a Gaussian plus Lorentzian fit overlaid. The effectiveness of our telluric line removal procedure can be judged from Figure 6, where all the telluric line profiles from the 2010–2011 observing season are compared with the same profiles after the telluric line removal. The marginal residual telluric emission seen near 0 km s^{-1} in Figure 6(b) is subsequently scattered over a range of ~85 km s^{-1} when the spectra are converted back into the LSR frame, further diluting any effect on the celestial emission.

After removal of the telluric lines, we performed a conventional folding of the spectra by averaging each channel with its corresponding reference-phase mate 15 MHz higher in frequency. This procedure lowers the noise by the square-root of two in all but the 60 end channels without mates; these channels were eliminated, reducing the final usable velocity coverage of the survey to ±47.5 km s^{-1}. Although the folding results in uniform noise reduction across the band, it leaves half-intensity negative image lines offset ±39 km s^{-1} from any positive emission. As we discuss next, nearly all large-scale summary maps and analyses of the survey require that the noise be suppressed by moment masking, a technique that also zeros the half-intensity negative images.

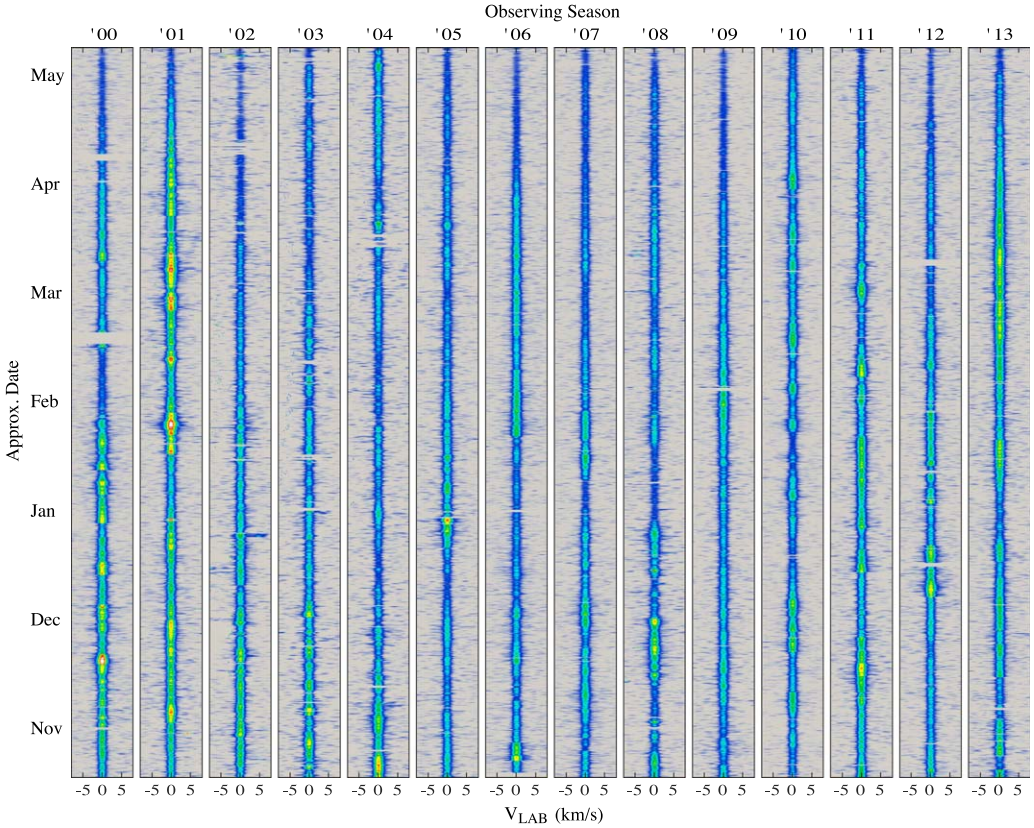

Figure 3. Summary of the mesospheric CO lines we observed in each spectrum. The lines are shifted in velocity to the laboratory frame and in intensity to the zenith. The lines are sorted vertically by scan number and horizontally by observing season. The dates on the left are only approximate because owing to weather and other delays, scan numbers did not increase linearly with time. The year noted at the top corresponds to the start of the observing season, which typically runs into May of the following year. Horizontal gaps in the stacked lines are due to ranges of scan numbers that were eliminated during the data processing and were subsequently repeated.

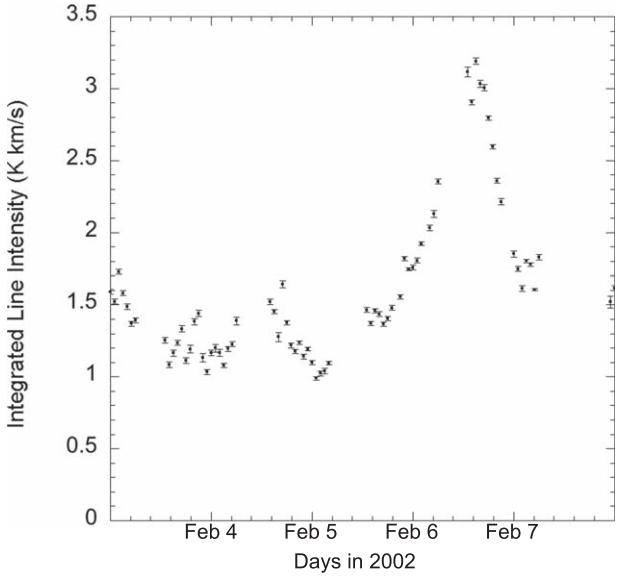

Figure 4. Integrated intensity of the mesospheric CO line at the zenith averaged in 1 hr bins during a five-day period in 2002 February. The error bars are 1σ based on the instrumental noise.

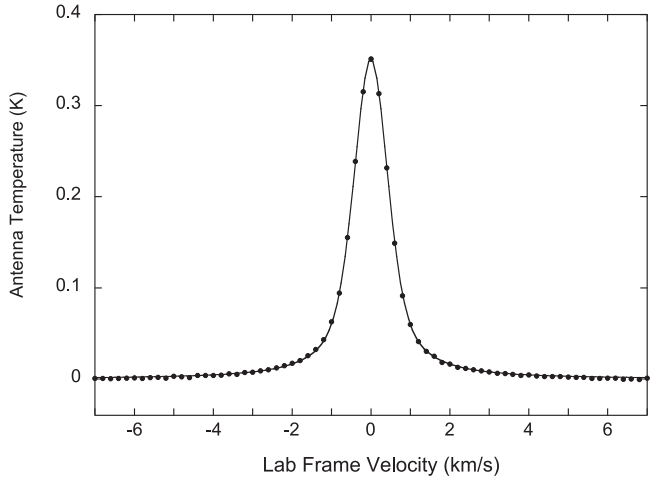

Figure 5. Average of all the mesospheric CO lines observed during the 2001–2002 season with the fit of a Gaussian plus Lorentzian function overlaid. As in Figure 3, the lines have been shifted in velocity to the laboratory frame and in intensity to the zenith. The Gaussian peak amplitude and dispersion are 0.167 ± 0.011 K and 0.410 ± 0.006 km s^{-1}, and the Lorentzian peak amplitude and width parameter are 0.185 ± 0.012 K and 0.622 ± 0.025 km s^{-1}. Both functions were assumed to be centered at 0 km s^{-1}.

Extracting all significant emission from the present survey was another serious challenge. The CO lines at high latitude are typically weak (∼0.5–1 K), narrow (∼1–2 km s^{-1}), and widely scattered. In a sky map created by simply integrating the final survey over all velocities (±47 km s^{-1}), nearly all such lines are lost in the noise. A common solution for this dilemma is to set all spectral channels below 3σ to zero before integrating ("clipping"), but this is also untenable for the present very large survey, for which over 3000 pure-noise spikes are expected above 4σ (assuming perfect Gaussian noise and perfect telluric

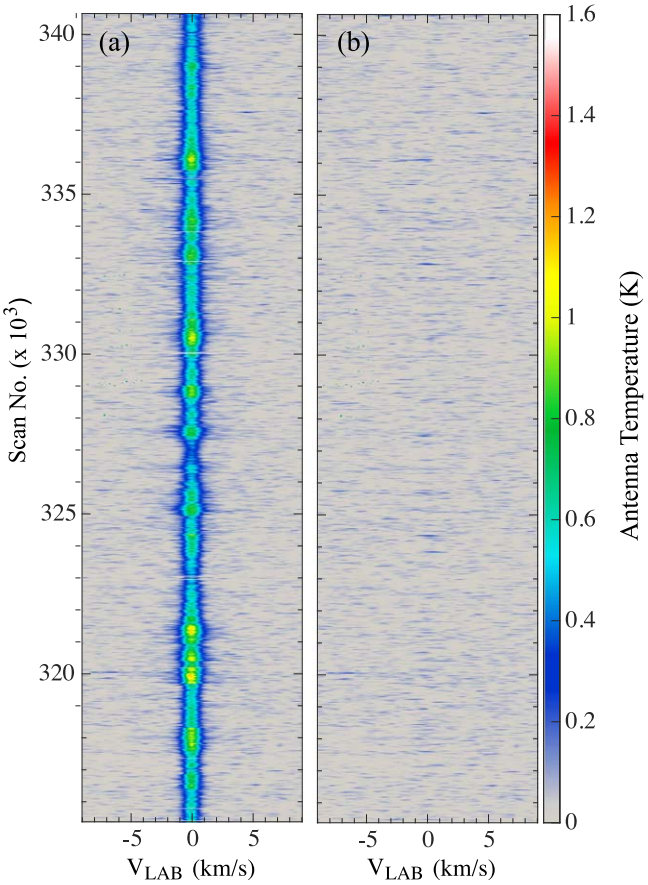

Figure 6. Mesospheric CO line profiles for the 2010–11 observing season, as in Figure 3, before (a) and after (b) the mesospheric line removal described in Section 3.

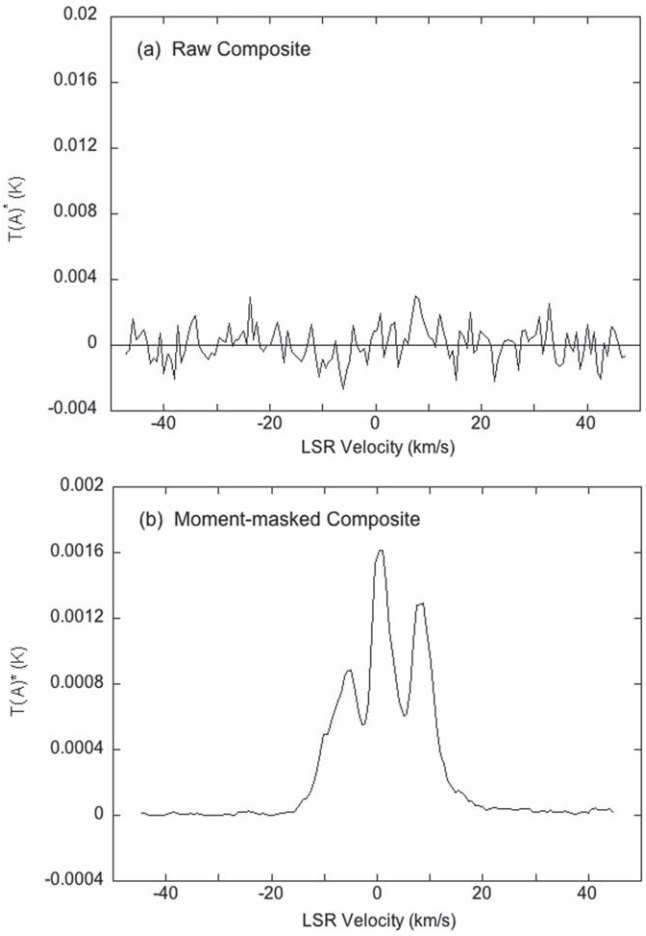

Figure 7. Demonstration of the ability of moment masking to reveal weak emission in a large survey. Average of all 382,202 of the new high-latitude CO spectra before (a) and after (b) moment masking was applied to the survey. Note that the emission evident in (b) is on an intensity scale that is 10 times lower than that in (a).

line removal). Consequently, to extract significant emission from the survey, we have adopted the moment-masking technique described in Dame (2011). Essentially, this is a refinement of the clipping method in which the coherence of the signal—determined from a smoothed version of the data cube—is considered in determining which peaks are real (and consequently not blanked). For the present survey, we smoothed the cube spatially to a resolution of $1/2°$ and in velocity to a resolution of 2.5 km s^{-1} and then blanked regions in the original cube corresponding to intensities lower than 5σ in the smoothed cube.

As one measure of the effectiveness of the moment masking, we show in Figure 7 composite spectra obtained by averaging all the individual spectra in the survey; the version in the top panel was derived from the raw spectra (after atmospheric line removal), and the version in the bottom panel shows the moment-masked spectra. Whereas no significant emission is evident in the raw composite, the moment composite reveals emission at all velocities within $\sim$15 km s^{-1} of zero, but on an intensity scale that is 10 times lower than that of the raw composite.

Of course, for essentially all large-scale CO studies, the present moment-masked survey must be combined with a moment-masked version of the DHT survey. This is especially true because the two surveys are interleaved spatially in a fairly complex way. The new survey covers all of the northern sky not covered by DHT, i.e., all of the component surveys shown in Figure 1 of DHT, except for survey 1, the low-resolution "superbeam" survey, which we reobserved. Moment-masked versions of the DHT component surveys, each optimized with their own set of masking parameters, have long been available online,[2] as has a combination of all these into a full DHT moment-masked cube. A combined cube consisting of the DHT and present surveys was used for all of the maps presented in the next section.

4. Summary Maps

A map of velocity-integrated CO intensity over the entire northern sky is shown in Figure 8. As just discussed, this map was derived by integrating the combined moment-masked cube over velocity. While the map reveals no large clouds at high latitude that were not already cataloged by the H&M survey, it provides the first detailed, unbiased maps of nearly all of them. In addition, it reveals dozens of smaller high-latitude clouds for the first time.

While every feature in Figure 8 derives from unmasked regions of the spectral line cube in which the total emission is in excess of 5σ (see Dame 2011), it is important to note that the noise in the map is not constant because different numbers of unmasked channels are summed over at each position.

[2] https://lweb.cfa.harvard.edu/rtdc/CO/IndividualSurveys/

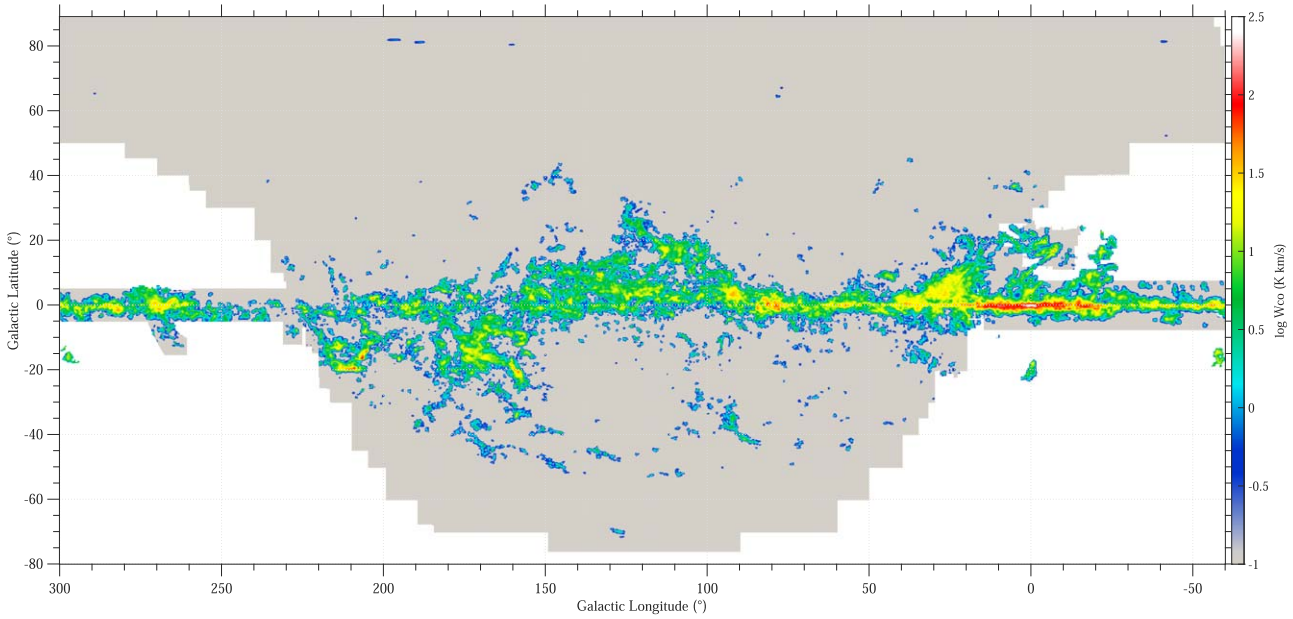

Figure 8. Velocity-integrated CO intensity over the entire northern sky. It was derived by integrating the combined moment-masked cube (No. 5 in Table 3) over velocity from −36 to 36 km s^{-1}, the full range over which significant emission is detected. For cosmetic purposes, the map was interpolated to 1/8° spacing and smoothed slightly by convolution with a 0.°3 Gaussian. The white area is unobserved.

(The data used to create this figure are available).

Table 2
Molecular Clouds in the Northern Sky at $|b| > 20°$

No.	l (deg)	b (deg)	Vel. (km s^{-1})	Δv (km s^{-1})	W_{CO} (K km s^{-1})	S_{CO} (K km s^{-1} deg^2)	N_{sig}
(1)	(2)	(3)	(4)	(5)	(6)	(7)	(8)
1	−41.50	52.25	−14.0	0.68	0.8	0.1	5
2	−40.00	81.25	23.8	0.67	0.8	0.1	5
3	−24.00	20.25	6.4	1.72	3.7	4.6	25
4	−21.50	22.50	2.6	2.14	13.4	13.7	60
5	−15.25	24.00	−0.8	2.70	14.5	4.1	30

Note. Cloud properties are as follows: (1) ID number, (2) Galactic longitude of the peak CO intensity, (3) Galactic latitude of the peak CO intensity, (4) LSR velocity from a Gaussian fit to the cloud's composite spectrum, (5) velocity dispersion from a Gaussian fit to the cloud's composite spectrum, (6) peak velocity-integrated intensity, (7) total CO luminosity, and (8) statistical significance of the total CO luminosity (assuming pure Gaussian noise of 0.18 K in 0.65 km s^{-1} channels).

(This table is available in its entirety in machine-readable form.)

Moreover, because the masking results in large areas of the map being set to zero (gray), any data artifacts such as those from imperfect atmospheric line removal, marginally bad channels, poor baseline fitting, or higher noise in regions of incomplete sampling will produce features in the map that appear to the eye as highly significant. We cannot rule out the possibility that a few small features in the map are produced by such artifacts.

We have partitioned the emission in Figure 8 into 198 discrete high-latitude clouds ($|b| > 20°$) and list their properties in Table 2. Here we define clouds as regions of contiguous emission, as indicated by the color-coding in Figure 9. While this approach is common and straightforward, it will inevitably partition some clouds from previous catalogs and combine others. The table includes each cloud's peak position and velocity-integrated intensity, its velocity and line width as determined from a Gaussian fit to its composite spectrum, its total CO luminosity integrated over sky area and velocity, and the statistical significance of this luminosity. Only clouds with a significance in excess of 3σ are included in Table 2.

Cloud masses are not included in the table because distances to most of the clouds are not known. For those with known distances, masses can be computed from their CO luminosities as

$$M(M_\odot) = 0.0013 L_{co}(\mathrm{K\ km\ s^{-1}\ deg^2})\, d(\mathrm{pc})^2, \qquad (1)$$

where we have adopted a CO-to-H_2 conversion factor of 2×10^{20} cm^{-2} (K km s^{-1})$^{-1}$ (Bolatto et al. 2013) and include a factor of 1.36 for heavy elements.

It is of interest to compare our clouds at $|b| > 30°$ with the high-latitude detections reported by H&M (Table 2 of Hartmann et al. and Table 1 of Magnani et al.). H&M report a total of 159 detections at positions on their 1° search grid. Of these, all but five overlap with or fall within ∼1° of our cataloged clouds. Of the five H&M detections not in or near our cataloged clouds, three show weak lines in our data at

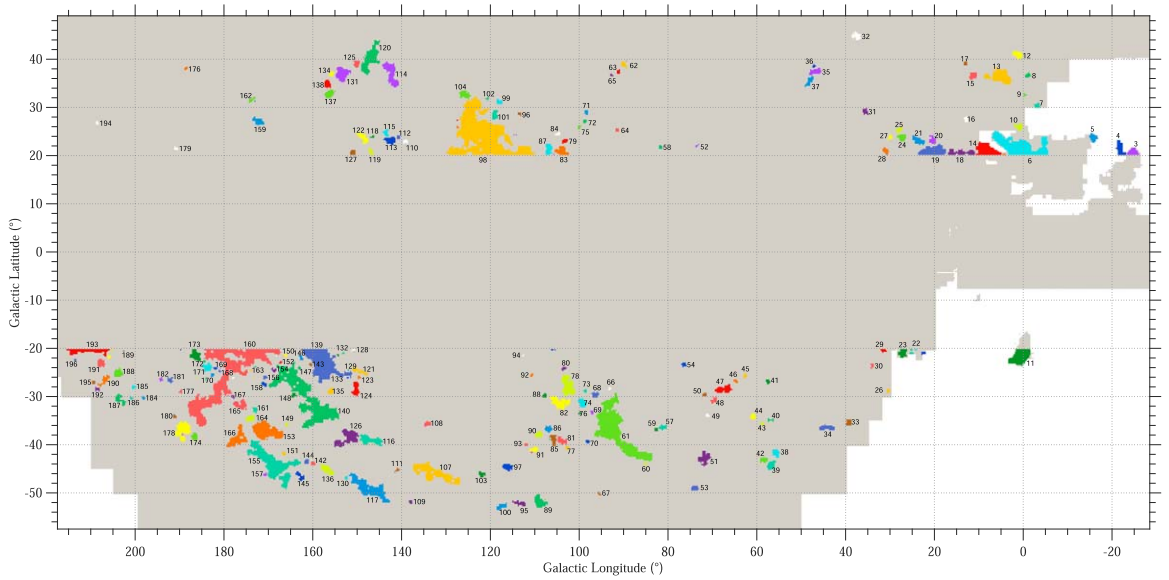

Figure 9. A finder chart for most of the molecular clouds we have identified in the northern sky at $|b| > 20°$ (Table 2). The colors here simply help to distinguish individual clouds. For clarity, we have zoomed in on the crowded regions of Figure 8. The small number of clouds outside the limits of this chart can be readily identified from Figure 8 and Table 2.

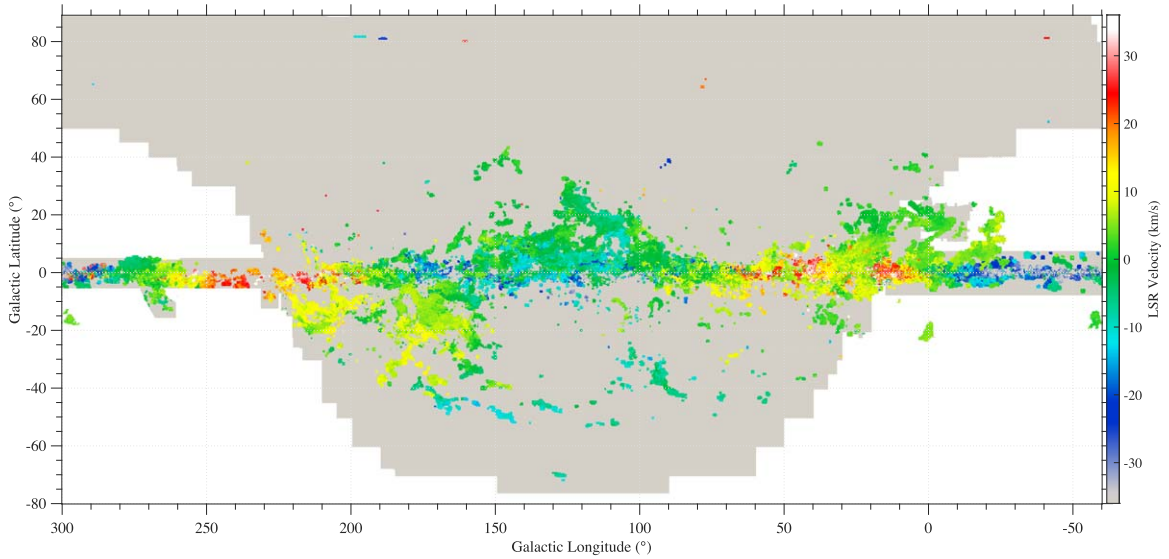

Figure 10. Map of the peak LSR velocity for all nonzero positions in Figure 8. It was derived from the combined moment-masked cube (No. 5 in Table 3). At $|b| > 20°$, the peak velocities should correspond closely to the mean cloud velocities given in Table 2. Near the Galactic plane, however, the emission is complex and the velocities extend beyond the range represented by the colors.

approximately the right velocity, but below our cloud significance threshold; the remaining two are at (139.2, −66.0) and (192.1, −55). On the other hand, fewer than half of our clouds in the region of the H&M survey are detected by that survey (39 of 100). Given the 16 times finer sampling of our survey, it is not surprising that many of our smaller clouds escaped detection by H&M.

Two perspectives on the velocity distribution of emission in our survey are given in Figures 10 and 11. The first is a spatial map of the velocity at the spectral peak, shaded by color over the range −36–36 km s^{-1}. Each position is independently shaded, so gradients across individual clouds can sometimes be seen. Because this figure was derived from the moment-masked cube and there is very rarely more than one emission line in any direction at high latitude, the velocity shading should correspond very closely to the velocities given in Table 2. In contrast, the emission near the plane is complex and extends beyond the range of the shading; still, a general change in sign is apparent across the cardinal directions of longitude.

The other perspective shown in Figure 11 was obtained by integrating the same moment-masked cube over all longitudes. Outlier clouds in velocity or latitude are labeled as in Table 2. Clouds 62, 63, and 65 near $v = -24$ km s^{-1} and $b = 38°$ constitute the well-known Draco complex (Mebold et al. 1985). Note that we find a number of other high-latitude clouds with velocities and latitudes comparable to Draco, but they are all significantly dimmer and presumably less massive.

As an additional summary of the cloud velocities, we show a histogram of their values in Figure 12. We find a mean value for the ensemble of −0.28 km s^{-1}, suggesting no net expansion or contraction of the local clouds, and a velocity dispersion of 9.5 km s^{-1}. Both of these values are in reasonable agreement

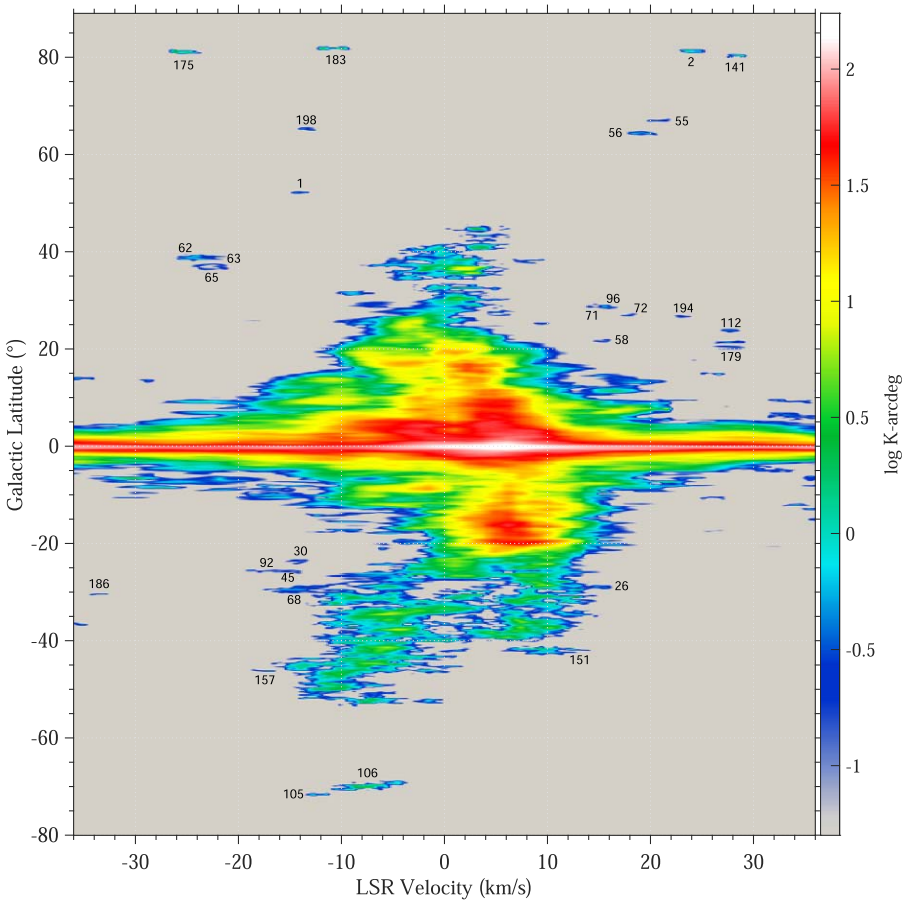

Figure 11. Latitude–velocity map of CO emission integrated over the full longitude range of the present survey (No. 5 in Table 3). Outlier clouds are identified by their numbers in Table 2.

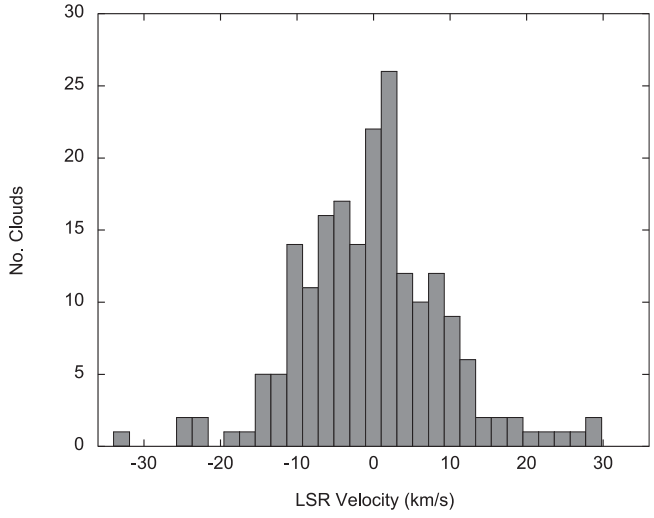

Figure 12. Histogram of the mean cloud velocities given in Table 2.

with those obtained in the same way from the H&M survey (-0.85 km s^{-1} and 7.4 km s^{-1}, respectively).

5. Data Products

Unlike all previous CO surveys and studies of the high-latitude sky, the utility of the present survey extends well beyond the summary maps and cloud catalog presented here because all 382,202 spectra can be made available in a single FITS-format data cube. In Table 3 we list five versions of the cube that are publicly available and discuss the advantages and drawbacks of each below. All of the cubes are on a rectangular Cartesian grid of velocity, longitude, and latitude.

Table 3
Publicly Available Spectral Line Data Cubes

No.	Name	Size (Mb)	Vel. Range (km s^{-1})	rms (K)
1	DT22_raw.fits	847	−47.1 to 86.2	0.26
2	DT22_folded.fits	545	−47.1 to 47.1	0.18
3	DT22_interp.fits	271	−47.1 to 47.1	0.18
4	DT22_masked.fits	285	−47.1 to 47.1	⋯
5	DT22+DHT_masked.fits	285	−47.1 to 47.1	⋯

Note. Cubes are available from the Radio Telescope Data Center (https://lweb.cfa.harvard.edu/rtdc/CO/NorthernSkySurvey/).

The first file contains only the observed spectra, without interpolation, folding, noise masking, or DHT spectra. These spectra provide the largest velocity coverage, but at the expense of higher noise than the folded spectra. Every real emission line appears twice in these spectra with opposite signs and separated by 39 km s^{-1}. To accommodate the gradually increasing longitude spacing with increasing latitude, the longitude spacing in this cube is $0\overset{\circ}{.}125$. Consequently, at $|b| < 50°$, only every other position in longitude is observed; at higher latitudes, it becomes every third position, then every fourth, and so on as prescribed in Table 1.

In file No. 2 the same spectra have been folded as described in Section 3. This lowers the noise to our target sensitivity of 0.18 K, but at the expense of 39 km s^{-1} in velocity coverage. In these spectra, every emission line has half-intensity negative image lines offset by ± 39 km s^{-1}.

While the first two files contain all of the observed spectra, they are not practical for most analyses owing to the large number of missing spectra on the $0\overset{\circ}{.}125$ longitude grid. In file No. 3 we have linearly interpolated the data in longitude and then compressed the longitude spacing to $0\overset{\circ}{.}25$ to match that of latitude. This is arguably the best file for working with the high-latitude survey alone, but without the benefits of moment masking or the addition of spectra from the DHT survey. Users should also keep in mind that because most of the spectra at the higher latitudes are interpolated, the noise there is highly correlated in longitude.

File No. 4 is a moment-masked version of the survey. In order for this technique to work successfully, the input survey must have uniform noise and sampling. Consequently, approximately a dozen regions typically 5°–10° in size lying along the decl. limit of the survey or along the interface with the DHT survey were deleted owing to undersampling; these were most often regions in which fewer than all four of the 1/2° interleaved grids were completed (Section 2). The moment masking as described by Dame (2011) employed 2.5 km s^{-1} smoothing in velocity and $0\overset{\circ}{.}5$ true-angle smoothing on the sky, and the masking/blanking was below a level of 5σ (0.11 K) in the smoothed cube. After masking, the velocity of every weak feature was compared with the velocity of the mesospheric line at the time of observation, and those that matched were eliminated as probable residuals from the mesospheric line removal.

Finally, file No. 5 is a combination of the moment-mask versions of the present survey (No. 4) and that of the DHT survey; the latter is itself a combination of several dozen of its component surveys, all moment-masked individually and available from the Radio Telescope Data Center. The velocity range of the cube is restricted to that of the present survey, and therefore higher-velocity emission in the DHT survey is not included.

Much of the data for this survey were obtained by several dozen Harvard undergraduate students who worked as observing assistants at night and on weekends; a few students were hired each observing season. Ordered chronologically, their names are Roxanne Lanzot, Graeme Wood, Adam Kampff, Stefan Ichim, Karin Sanstrom, Bogdan Grigorescu, Ryan Carlon, Mario Garcia, Liviu Stirbat, Manuel Aguilar, Varun Narendr, Jeffrey Blair, James Grundy, Jonathan Aguilar, Yizi Shang, Ming Li, Sorin Floti, Gabe Franggkis, Kate Caputo, Rena Mei, Daniel Henderson, Sameer Tyagi, and David Paiva. In addition, substantial help with the observing and telescope operations were provided by Jodie Dalton (Harvard Law School), Alex Wilson (graduate student, Univ. Bristol), Ester Aguti (graduate student, Univ. Bristol), Muzzez Lohmiller (CfA staff), Joseph Megnia (Boston Univ.), and Tülün Ergin (CfA Fermi postdoc). We gratefully acknowledge financial support from the Scholarly Studies Program of the Smithsonian Institution, the NASA/GLAST Guest Investigator Program, and the Stanford Linear Accelerator Center.

ORCID iDs

T. M. Dame https://orcid.org/0000-0003-0109-2392

References

Bolatto, A. D., Wolfire, M., & Leroy, A. K. 2013, ARA&A, 51, 207
Cohen, R. S., Dame, T. M., Garay, G., et al. 1988, ApJL, 331, L95
Dame, T. M. 2011, arXiv:1101.1499
Dame, T. M., Hartmann, Dap., & Thaddeus, P. 2001, ApJ, 547, 792, (DHT)
Dame, T. M., Koper, E., Israel, F. P., & Thaddeus, P. 1993, ApJ, 418, 730
Dame, T. M., & Thaddeus, P. 2011, ApJL, 734, L24
Désert, F. X., Bazell, D., & Boulanger, F. 1988, ApJ, 334, 815
de Zafra, R., & Muscari, G. 2004, JGRD, 109, D06105
Downes, D. 1989, LNP, 333, 351
Forkman, P., Christensen, O. M., Eriksson, P., Urban, J., & Funke, B. 2012, AMT, 5, 2827
Hartmann, D., Magnani, L., & Thaddeus, P. 1998, ApJ, 492, 205
Kutner, M. L. 1978, ApL, 19, 81
Lallement, R., Snowden, S., Kuntz, K. D., et al. 2016, A&A, 595, A131
Magnani, L., Blitz, L., & Mundy, L. 1985, ApJ, 295, 402
Magnani, L., Hartmann, D., Holcomb, S. L., Smith, L. E., & Thaddeus, P. 2000, ApJ, 535, 167
Mebold, U., Cernicharo, J., Velden, L., et al. 1985, A&A, 151, 427
Penzias, A. A., & Burrus, C. A. 1973, ARA&A, 11, 51
Planck Collaboration 2016, A&A, 594, A10
Solomon, S., Garcia, R. R., Olivero, J. J., et al. 1985, JAtS, 42, 1072